RESEARCH ARTICLE | NOVEMBER 18 2025

Subgrid-scale model derived from the lattice Boltzmann equation **6**

K. Yamamoto (山本惠一) ■ 📵



Physics of Fluids 37, 115148 (2025) https://doi.org/10.1063/5.0294087





Articles You May Be Interested In

Lattice Boltzmann-based subgrid-scale modeling of fully developed turbulent pipe flow

Physics of Fluids (August 2025)

Dynamic nonlocal passive scalar subgrid-scale turbulence modeling

Physics of Fluids (October 2022)

A new subgrid characteristic length for turbulence simulations on anisotropic grids

Physics of Fluids (November 2017)



Physics of Fluids

Special Topics Open for Submissions

Learn More



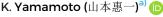
Subgrid-scale model derived from the lattice Boltzmann equation ()

Cite as: Phys. Fluids **37**, 115148 (2025); doi: 10.1063/5.0294087 Submitted: 1 August 2025 · Accepted: 17 October 2025 · Published Online: 18 November 2025









AFFILIATIONS

PILLAR Corporation, 7-1, Shinmachi 1-chome, Nishi-ku, Osaka 550-0013, Japan

^{a)}Author to whom correspondence should be addressed: keiichi.yamamoto@pillar.co.jp

ABSTRACT

The cumulant lattice Boltzmann method (LBM), a variant of LBM, inherently exhibits an implicit large-eddy simulation (LES) effect. To facilitate subgrid-scale (SGS) turbulence modeling, we analyze the error terms of the lattice Boltzmann equation and deductively derive a novel, parameter-free SGS model (hereafter the kinetic model). A priori tests using direct numerical simulation (DNS) data were conducted for both the absolute magnitude of the SGS volume force and the SGS dissipation. These tests show that, while the gradient model (GM) performs slightly better in terms of local correlation and mean absolute error, the kinetic model (KM) provides closer agreement with DNS in the global distribution and large-scale coherence of the SGS fields. In this sense, the KM demonstrates superior capability for capturing the overall structure of turbulent energy transfer. In addition, *a posteriori* validation using LESs of the Taylor–Green vortex confirms that the KM reproduces the dissipation rate and energy spectra more accurately than the GM while maintaining numerical stability. Thus, the present study evaluates the model both *a priori* and *a posteriori*, confirming its effectiveness and robustness.

© 2025 Author(s). All article content, except where otherwise noted, is licensed under a Creative Commons Attribution (CC BY) license (https://creativecommons.org/licenses/by/4.0/). https://doi.org/10.1063/5.0294087

I. INTRODUCTION

The lattice Boltzmann method (LBM)¹ has emerged as a mainstream approach in fluid mechanics in recent years, serving as an alternative to directly solving the Navier–Stokes equations.² In the LBM, the velocity space of fluid particles is discretized into a finite set of velocity vectors, and the distribution function represents the number of fluid particles associated with each velocity vector. The lattice Boltzmann equation (LBE) governs the evolution of this distribution function. Although LBM introduces minor discretization errors, it has been mathematically proven to reproduce solutions of the Navier– Stokes equations.³

LBM is categorized into various models based on the treatment of the collision term. Among these, the cumulant collision model has gained particular attention for its computational stability and accuracy. This model significantly enhances numerical stability in turbulent flow simulations by modifying only the collision process. Moreover, it exhibits high computational reproducibility without requiring explicit turbulence models such as the Smagorinsky model. This observation suggests that the cumulant LBM inherently incorporates the effects of a subgrid-scale (SGS) turbulence model. This phenomenon is typically described as implicit large-eddy simulation (ILES), attributed to numerical truncation errors, although the underlying mechanism remains

unclear. 5 Previous studies, notably those by Chen *et al.*, $^{7-9}$ have extensively discussed the ILES characteristics of LBM through numerical investigations. However, these studies did not provide a direct theoretical derivation of SGS terms from the underlying LBE.

In contrast, the present study develops a deductive framework for SGS turbulence modeling based on a systematic error analysis of the cumulant LBE. Two guiding hypotheses are introduced: (1) the error terms of the LBE inherently contain physically relevant corrections analogous to SGS turbulence models, and (2) only those error terms satisfying spatial rotational symmetry and Galilean invariance should be retained, while nonphysical anisotropic contributions are excluded. Applying these principles yields an explicit expression for an SGS volume force (hereafter referred to as the kinetic model), which is parameter-free and derived purely from the LBE.

It is essential to clarify that the present model is deductively derived from the LBE. Its performance is first evaluated through *a priori* tests using filtered data from the Johns Hopkins Turbulence Database (JHTDB), which allow direct assessment of the SGS term against high-fidelity direct numerical simulation (DNS) data while avoiding numerical contamination. In these tests, the proposed model is benchmarked against the well-established gradient SGS model, and comparisons are made in terms of correlation coefficients, mean

absolute errors (MAEs), and contour patterns of the SGS volume force. The results demonstrate that the gradient model (GM) performs slightly better in terms of local correlation and mean absolute error, and the kinetic model (KM) provides closer agreement with DNS in the global distribution and large-scale coherence of the SGS fields.

In addition to the *a priori* analysis, *a posteriori* validation is conducted in large-eddy simulations of the Taylor–Green vortex (TGV) at Re = 1600. These simulations confirm that the kinetic model reproduces the dissipation rate and energy spectra more accurately than the gradient model while maintaining numerical stability.

The structure of this paper is as follows. After outlining the guiding hypotheses and the theoretical framework used to derive the SGS model, we present both *a priori* validation using DNS data and *a posteriori* validation using large-eddy simulation (LES) of the Taylor–Green vortex. The paper concludes with a summary of accuracy, stability, and future perspectives.

II. METHODS

We propose the following two hypotheses to guide SGS model development:

- Hypothesis 1: The LBM is analogous to the kinetic theory of gas molecules. Therefore, the error terms inherent in the LBE are hypothesized to contain physically relevant corrections analogous to SGS turbulence models.
- 2. Hypothesis 2: The LBM operates using a finite set of discrete velocity basis vectors arranged in fixed directions. As a result, the error terms may include components that violate spatial rotational symmetry and/or Galilean invariance. We explicitly eliminate nonphysical terms that violate spatial rotational symmetry and/or Galilean invariance from the derived SGS corrections.

These hypotheses form the foundation of our approach. We start from the following LBE, adopt the D3Q27 velocity basis, ¹¹ and apply established expansion theories, ^{12,13}

$$f_i(x + c_i \delta_t, t + \delta_t) - f_i(x, t) = -\frac{1}{\omega} (f_i - f_i^{eq}),$$
 (1)

where f_i denotes the distribution function of the ith discrete velocity, x is the spatial coordinate, f_i^{eq} is the equilibrium function, t is the time coordinate, and ϕ is the single-relaxation-time (SRT) parameter.

The macroscopic governing equations, expanded up to the order of Δ^2 (where Δ represents the mesh size), are presented later. For brevity, intermediate derivations are omitted, and only the final results are shown in Eq. (2). A detailed derivation is presented in the Appendix,

$$\begin{split} \frac{\partial u_{\alpha}}{\partial t} + u_{\beta} \frac{\partial u_{\alpha}}{\partial x^{\beta}} &= -\frac{\partial}{\partial x^{\alpha}} \left(\frac{p}{\rho} \right) + \nu \sum_{\beta} \frac{\partial}{\partial x^{\beta}} \left(\frac{\partial u_{\beta}}{\partial x^{\alpha}} + \frac{\partial u_{\alpha}}{\partial x^{\beta}} \right) \\ &- \frac{\Delta^{2}}{12} \left\{ \frac{\partial}{\partial x^{\alpha}} \sum_{\gamma,\mu} \frac{\partial u_{\mu}}{\partial x^{\gamma}} \frac{\partial u_{\gamma}}{\partial x^{\mu}} + 2 \frac{\partial}{\partial x^{\alpha}} \sum_{\gamma} \frac{\partial}{\partial x^{\gamma}} \frac{\partial}{\partial x^{\gamma}} \left(\frac{p}{\rho} \right) \right\} \\ &- \frac{\Delta^{2}}{12} \left(\frac{\partial}{\partial x^{\alpha}} \right)^{3} u_{\alpha}^{2} - \frac{\nu \Delta^{2}}{6} \left\{ \sum_{\beta,\gamma} \frac{\partial}{\partial x^{\beta}} \frac{\partial}{\partial x^{\beta}} \frac{\partial}{\partial x^{\gamma}} \frac{\partial}{\partial x^{\gamma}} u_{\alpha} \right. \\ &- 2 \left(\frac{\partial}{\partial x^{\alpha}} \right)^{4} u_{\alpha} \right\}, \end{split}$$
(2)

where u represents the macroscopic velocity of the fluid; α , β , and γ are vector components; ρ represents density; p represents pressure; and ν represents kinematic viscosity. Notably, in Eq. (2), summation is not applied solely over the index α .

The expansion theories presented in Refs. 12 and 13 yield mathematically equivalent results. However, unlike Ref. 12, the expansion method in Ref. 13 implies that the error terms may inherently contain correction terms analogous to subgrid-scale turbulence models.

Next, based on Hypothesis 2, we examine each term in relation to spatial rotational symmetry and Galilean invariance to identify which terms comply with these properties. Among the terms on the right-hand side of Eq. (2), those associated with the anisotropic tensor ¹⁴ do not meet these symmetry requirements. The volume force of the SGS model that preserves symmetry is expressed in the following equation:

$$F_{V,\alpha}^{KM} = -\frac{\Delta^{2}}{12} \left\{ \frac{\partial}{\partial x^{\alpha}} \sum_{\gamma,\mu} \frac{\partial \overline{u}_{\mu}}{\partial x^{\gamma}} \frac{\partial \overline{u}_{\gamma}}{\partial x^{\mu}} + 2 \frac{\partial}{\partial x^{\alpha}} \sum_{\gamma} \frac{\partial}{\partial x^{\gamma}} \frac{\partial}{\partial x^{\gamma}} \left(\frac{\overline{p}}{\rho} \right) \right\}$$
$$-\frac{\nu \Delta^{2}}{6} \sum_{\beta,\gamma} \frac{\partial}{\partial x^{\beta}} \frac{\partial}{\partial x^{\beta}} \frac{\partial}{\partial x^{\gamma}} \frac{\partial}{\partial x^{\gamma}} \frac{\partial}{\partial x^{\gamma}} \overline{u}_{\alpha}. \tag{3}$$

In the present study, the SGS volume force is used directly rather than being converted back into a stress tensor. Although the divergence $F_i = -\partial_j \tau_{ij}$ is uniquely defined, the stress tensor itself is not, since adding an isotropic component $q\delta_{ij}$ leaves F_i unchanged. Using the force-based formulation avoids this ambiguity and provides a direct connection to the resolved energy budget. Therefore, both the *a priori* tests with filtered DNS data and the *a posteriori* tests within LES employ the volume force as derived.

III. RESULTS

A. A priori validation

1. Validation approach

We outline the *a priori* test used to verify the SGS model. This *a priori* test must include a computation of the volume force, which is the correct data, from the DNS in advance, and the following Eq. (4) is used for this computation:

$$F_{V,\alpha}^{DNS} = -\sum_{\beta} \frac{\partial}{\partial x^{\beta}} \tau_{\alpha\beta}$$

$$= -\sum_{\beta} \frac{\partial}{\partial x^{\beta}} (\overline{u_{\alpha}u_{\beta}} - \overline{u}_{\alpha} \cdot \overline{u}_{\beta}), \tag{4}$$

where $\tau_{\alpha\beta}$ is the turbulent stress, which is defined by averaging the velocity components in the coarse grid.

A top-hat filter¹⁵ was used for coarse-graining, and the turbulent stress was first computed using the fine grid value included in the coarse grid. Here, we adopted 3Δ , 5Δ , 9Δ , and 17Δ for the coarse-graining mesh for computational convenience, where Δ is the mesh size of the DNS. The volume force calculation required a differential operation on the turbulent stress, which was performed using differences across coarse grid points (i.e., filtered DNS). The DNS data used were the FORCED ISOTROPIC TURBULENCE DATA SET from the Johns Hopkins Turbulence Databases (JHTDB). ¹⁶

To generate the volume force from the SGS model, a coarsegrained representation of the fluid field was computed by first applying

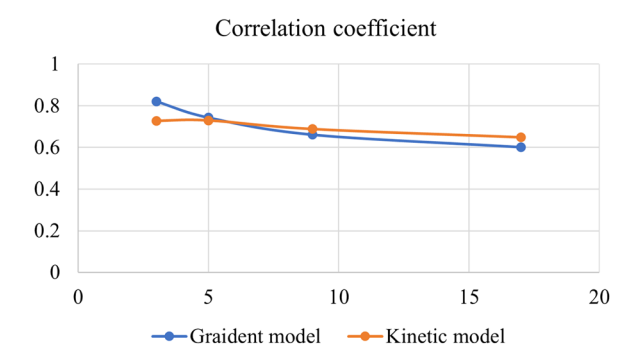


FIG. 1. Correlation coefficients between the SGS volume force predicted by the kinetic model and the gradient model, and the reference obtained from filtered DNS data (JHTDB). This comparison is conducted as an *a priori* test using DNS data only, without any LBM simulations.

a top-hat filter to the velocity and pressure fields in the DNS. A differential operation was then performed using differences across the coarse grid points, following each model's specific formulation.

2. Benchmarking model accuracy

We evaluated the model accuracy by comparing the correlation coefficients and MAEs of the gradient in Eq. (5) and kinetic in Eq. (3) models relative to the filtered DNS data. The gradient model, used as a benchmark in this study, is recognized as one of the most accurate models for *a priori* testing, ¹⁷ capable of capturing the structural behavior of the turbulence stress tensor with high precision,

$$F_{V,\alpha}^{GM} = -\frac{\Delta^2}{12} \sum_{\beta} \frac{\partial}{\partial x^{\beta}} \sum_{\gamma} \frac{\partial \overline{u}_{\alpha}}{\partial x^{\gamma}} \frac{\partial \overline{u}_{\beta}}{\partial x^{\gamma}}.$$
 (5)

We employed the FORCED ISOTROPIC TURBULENCE DATA SET¹⁶ from the JHTDB to compute the magnitude of the volume force on a cross-sectional plane defined by t = 10, $x1 = [0, 2\pi]$, $x2 = [0, 2\pi]$, and $x3 = \pi$. The corresponding values of each statistical quantity are presented in Figs. 1 and 2.

The X-axis in each figure represents the coarse-graining ratio based on the DNS mesh size. For example, a value of 17 indicates that the volume force was computed using both the gradient and kinetic models with data that had been coarse-grained over a $17 \times 17 \times 17 = 4913$ -point volume. However, to compute the filtered DNS reference, the turbulent stress must still be derived from the original DNS resolution, regardless of the extent of coarse-graining. The correlation coefficients for both models showed moderate yet significant correlation (\approx 0.7) with the filtered DNS data. However, the MAE of the kinetic model was consistently lower than that of the gradient model, indicating superior performance by the kinetic model (Figs. 1 and 2). To visualize these findings, we examined the absolute value of the volume force on a mesh of size 5Δ using contour plots. These visualizations are shown in Figs. 3-5. The contours confirm that the correction in the gradient model was weaker than that of the filtered DNS data. By contrast, the size and distribution of the volume force in the kinetic model closely matched those of the filtered DNS.

We further evaluate the distribution of subgrid-scale (SGS) dissipation predicted by the kinetic model and the gradient model (GM).

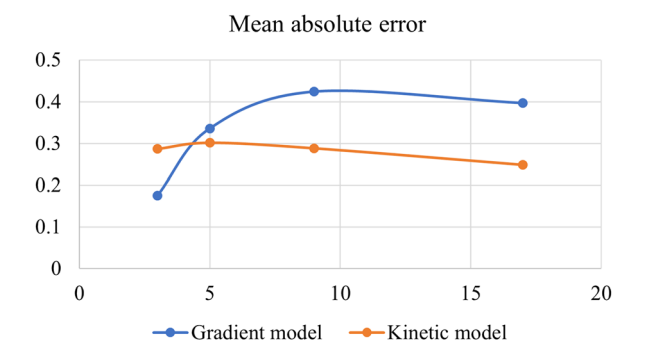


FIG. 2. Mean absolute errors (MAEs) of the SGS volume force components predicted by the kinetic and gradient models, relative to the reference from filtered DNS data (JHTDB). These results are obtained exclusively from an *a priori* evaluation, with no direct LBM simulations involved.

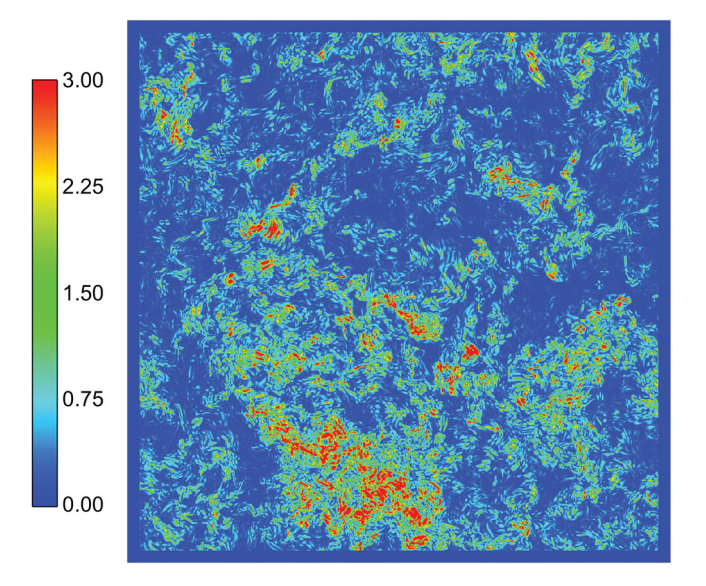


FIG. 3. Contour of the absolute volume force at mesh size $5\,\Delta$ based on the filtered DNS (JHTDB). This contour is treated as the reference data.

This analysis provides a more physically grounded validation, since dissipation is a key quantity governing energy transfer across scales in large-eddy simulation (LES).

In addition to the statistical comparison of model accuracy, it is also important to clarify how the proposed SGS corrections are connected to the turbulent energy transfer across scales. The link between the proposed SGS corrections and turbulent energy transfer can be clarified through the resolved kinetic energy budget. The SGS volume force is defined as

$$F_i = -\partial_i \tau_{ij}, \tag{6}$$

and its contribution to the time evolution of the resolved kinetic energy

$$E(t) = \frac{1}{2V} \int_{\Omega} \overline{u}_i \overline{u}_i \, dV \tag{7}$$

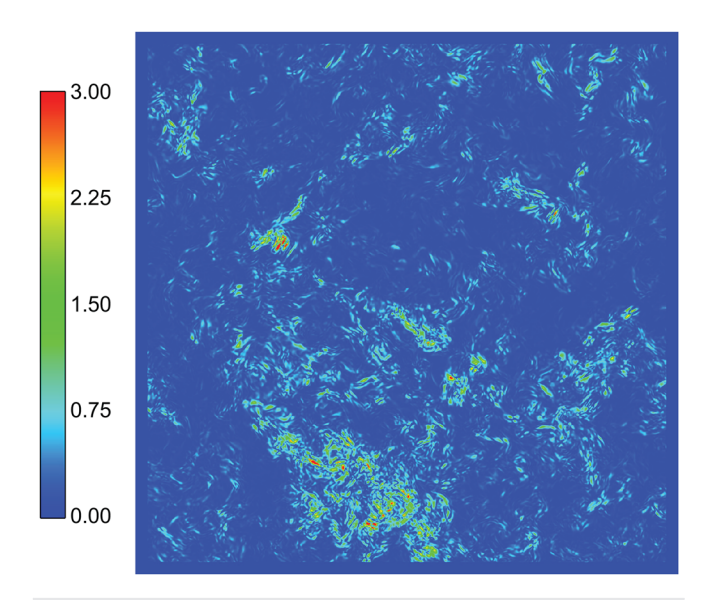


FIG. 4. Contour of the absolute volume force at mesh size $5\,\Delta$ based on the gradient model. The correction in the gradient model was weaker than that in the filtered DNS data.

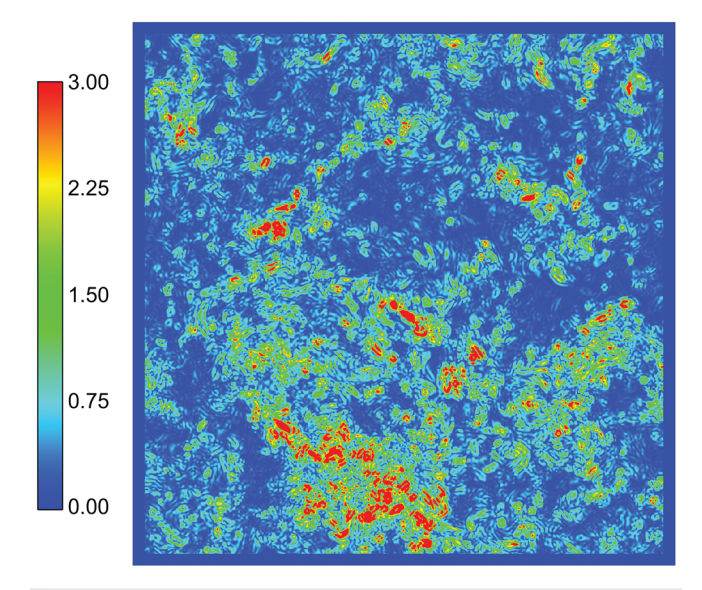


FIG. 5. Contour of the absolute volume force at mesh size $5\,\Delta$ based on the kinetic model (correction terms only). The results are validated against filtered DNS (JHTDB) in an *a priori* test, without any LBM simulations. The distribution of the volume force in the kinetic model closely matched that of the filtered DNS.

is written as

$$\begin{split} \frac{dE}{dt} &= -\frac{1}{V} \int_{\Omega} \nu \, \overline{S}_{ij} \overline{S}_{ij} \, dV + \frac{1}{V} \int_{\Omega} \overline{u}_i \, F_i \, dV \\ &- \frac{1}{V} \int_{\partial \Omega} \left(\overline{p} \, \overline{u}_i n_i + \frac{1}{2} \, \overline{u}_i \overline{u}_i \, \overline{u}_j n_j - \nu \, \overline{u}_i \, \partial_j \overline{u}_i \, n_j \right) \, dS. \end{split} \tag{8}$$

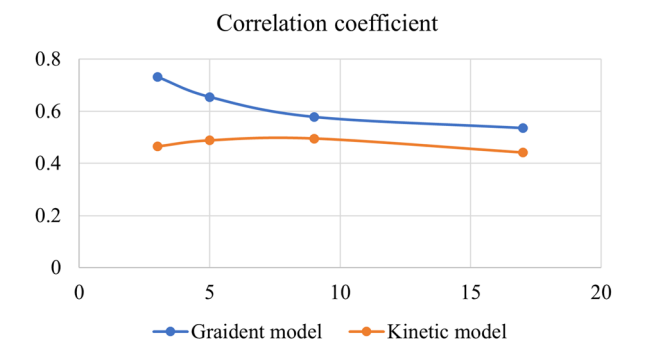


FIG. 6. Correlation coefficients of SGS dissipation predicted by the gradient model and the kinetic model, compared with the reference obtained from filtered DNS data (JHTDB). The comparison is performed as an *a priori* test using various coarsegraining ratios.

By integration by parts,

$$\frac{1}{V} \int_{\Omega} \overline{u}_i F_i \, dV = -\frac{1}{V} \int_{\Omega} \tau_{ij} \, \partial_j \overline{u}_i \, dV + \frac{1}{V} \int_{\partial \Omega} (\tau_{ij} \overline{u}_i) n_j \, dS. \tag{9}$$

For periodic domains or vanishing-flux boundaries, the surface term vanishes, and we obtain

$$\frac{1}{V} \int_{\Omega} \overline{u}_i F_i \, dV = -\frac{1}{V} \int_{\Omega} \tau_{ij} \, \overline{S}_{ij} \, dV, \tag{10}$$

where $\overline{S}_{ij}=\frac{1}{2}(\partial_i\overline{u}_j+\partial_j\overline{u}_i)$ is the resolved strain-rate tensor. Thus, the SGS dissipation is defined as

$$\varepsilon_{\text{SGS}} = -\langle \tau_{ii} \overline{S}_{ii} \rangle = \langle \overline{u}_i F_i \rangle.$$
 (11)

If $\varepsilon_{SGS}>0$, energy flows from resolved scales to subgrid scales (dissipation), while if $\varepsilon_{SGS}<0$, energy flows in the opposite direction (backscatter). This demonstrates that the proposed force-based SGS corrections directly govern the balance of turbulent energy transfer.

Figures 6 and 7 show the correlation coefficient and mean absolute error (MAE) of the dissipation field. It is observed that, in terms of local statistics, the GM exhibits higher correlation and lower MAE with respect to the filtered DNS data. In this sense, GM appears more advantageous for pointwise prediction accuracy.

However, visual inspection of the spatial distribution provides a different perspective. The contour maps in Figs. 8–10 compare the dissipation fields of DNS, GM, and KM. While GM exhibits higher pointwise accuracy, the KM produces a global pattern more consistent with the DNS distribution.

To quantify this global behavior, Fig. 11 presents the circular directional autocorrelation function (ACF) 18,19 of the dissipation field in the *y*-direction. Here, the KM shows closer agreement with DNS compared to the GM, which tends to retain spurious correlations at larger separations. This indicates that, although the GM is more accurate locally, the KM reproduces the large-scale structure of dissipation more faithfully. Similar tendencies were also confirmed for each component of the SGS volume force.

In summary, the present *a priori* dissipation test highlights a complementary behavior: the GM performs better in terms of local correlation and MAE, whereas the KM better captures the global distribution and large-scale coherence of SGS dissipation. These

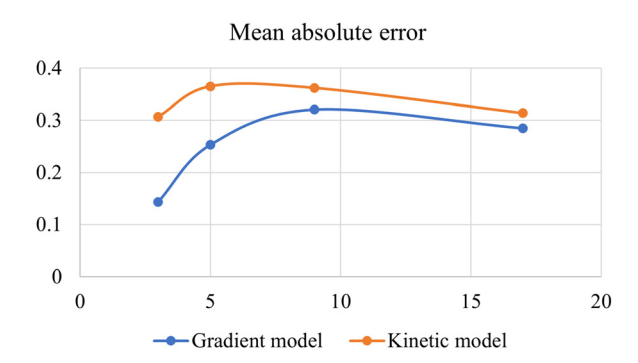


FIG. 7. Mean absolute errors (MAEs) of SGS dissipation predicted by the GM and KM, relative to filtered DNS data (JHTDB). The results are obtained from a *priori* tests at different coarse-graining ratios.

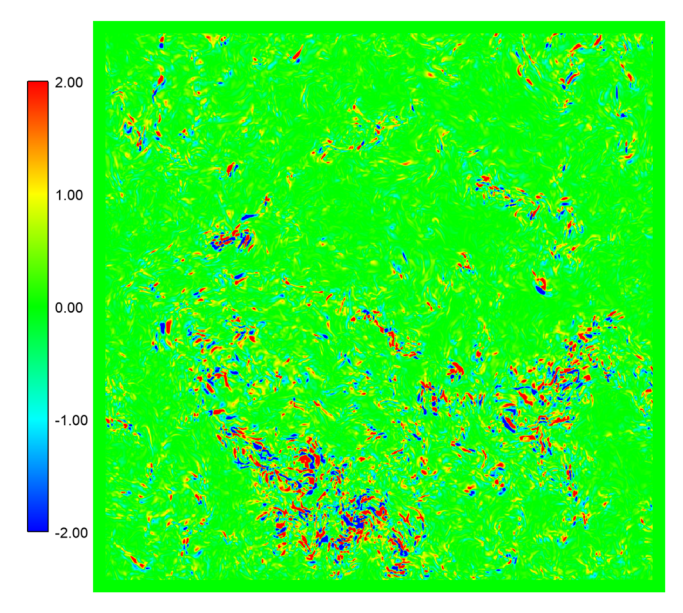


FIG. 8. Contour of SGS dissipation at coarse-graining ratio 5Δ based on filtered DNS data (JHTDB). This distribution is treated as the reference field for comparison.

tendencies were also observed consistently in each component of the volume force.

Ultimately, the decisive assessment of predictive capability must rely on *a posteriori* tests, where numerical stability, nonlinear feedback, and long-time energy transfer are all taken into account.

B. A posteriori validation

1. Validation approach (Taylor-Green vortex, Re=1600)

We compare (i) the time evolution of the total dissipation rate $\varepsilon(t)$ and (ii) the kinetic energy spectrum E(k) from the LES solutions. The definition of the box-averaged total dissipation rate is used,

$$\varepsilon = -\frac{\mathrm{d}E}{\mathrm{d}t},\tag{12}$$

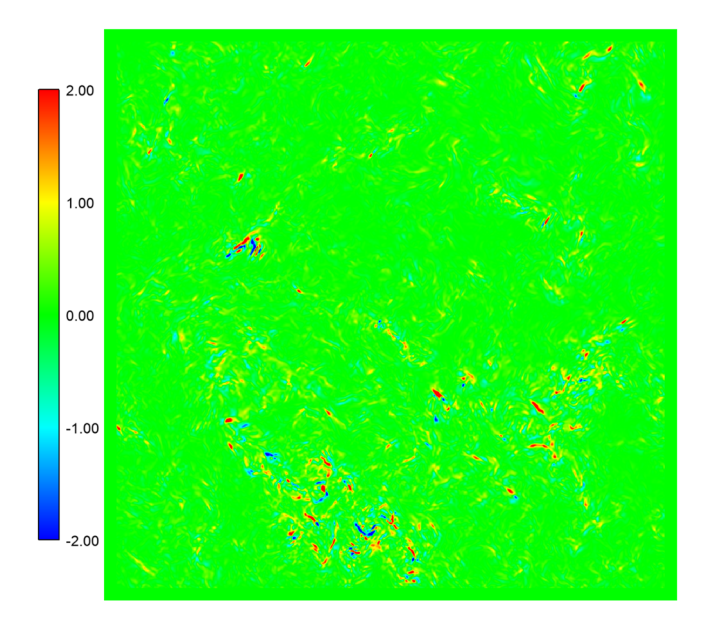


FIG. 9. Contour of SGS dissipation at coarse-graining ratio 5Δ predicted by the gradient model. The local intensity is captured, but the global distribution deviates from DNS

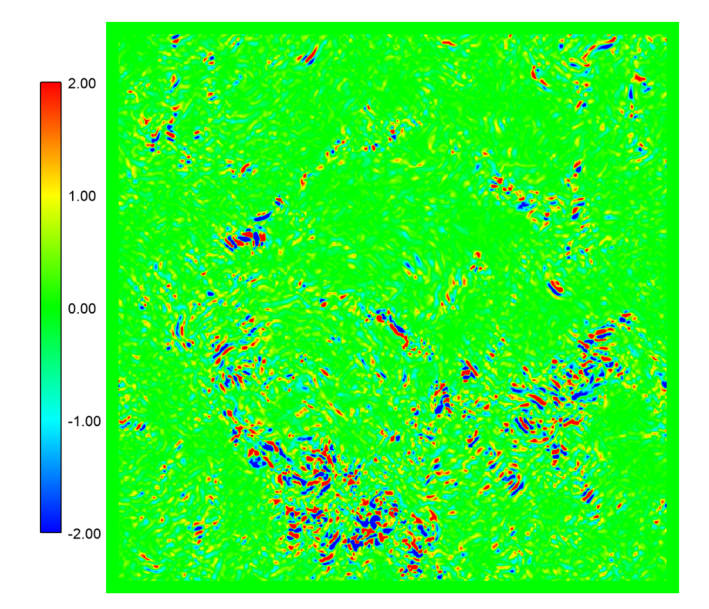


FIG. 10. Contour of SGS dissipation at coarse-graining ratio 5Δ predicted by the kinetic model. The global distribution more closely resembles the DNS reference compared with the GM.

$$E = \frac{1}{V} \int_{\Omega} \frac{1}{2} \, \overline{u}_i \, \overline{u}_i \, dV. \tag{13}$$

Here, V is the domain volume and \overline{u}_i is the resolved velocity. The energy spectra E(k) are computed with the standard OpenFOAM²⁰ functionObject energySpectrum.

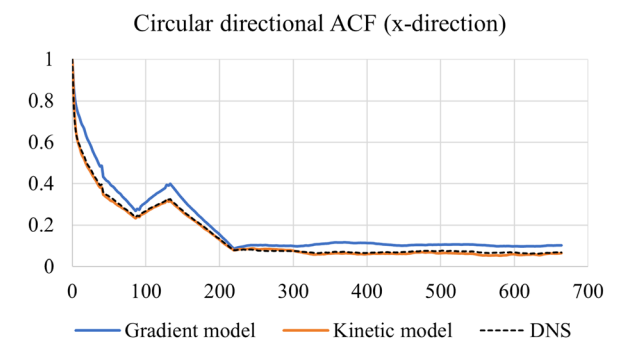


FIG. 11. Circular directional autocorrelation function (ACF) of SGS dissipation in the x-direction. The horizontal axis denotes the lag (the amount of spatial shift in the image). The KM shows closer agreement with DNS than the GM, which retains spurious correlations at larger separations.

The *a posteriori* calculations of the Taylor–Green vortex (TGV) at $Re = 1600^{10}$ are performed under the following conditions:

- Code/version: OpenFOAM v2212.
- Solver: pisoFoam (incompressible, transient).
- **Grids:** uniform Cartesian meshes with N^3 cells, N = 64.
- Spatial discretization (finite volume method, FVM): interpolation from cell centers to face centers uses fourth-order (cubic) schemes.
- Time integration: second-order backward implicit (backward).
- Time step: $\Delta t = 1.0 \times 10^{-3}$ s.
- **Domain:** periodic cube, $-\pi L \le x, y, z \le \pi L$.
- Boundary conditions: periodic in all three directions.
- Reynolds number and viscosity: $Re = U_0 L/\nu = 1600 \Rightarrow \nu = 6.25 \times 10^{-4}$ (nondimensional units).

Unless otherwise stated, spatial and temporal averages are volume-integrated over the full periodic box.

2. Benchmarking model accuracy

Figure 12 shows the volume-averaged dissipation $\varepsilon(t)$. The DNS peak occurs at $t_{\rm p}^{\rm DNS}=8.97~{\rm s}$ with $\varepsilon_{\rm p}^{\rm DNS}=1.286\times10^{-2}$. The KM peaks at $t_{\rm p}=8.673~{\rm s}$ ($-0.30~{\rm s}$ vs DNS) with $\varepsilon_{\rm p}=1.316\times10^{-2}$ (+2.4%). The GM peaks at $t_{\rm p}=8.152~{\rm s}$ ($-0.82~{\rm s}$) with $\varepsilon_{\rm p}=1.331\times10^{-2}$ (+3.5%). Smagorinsky (SM): $t_{\rm p}=8.447~{\rm s}$ ($-0.52~{\rm s}$) and $\varepsilon_{\rm p}=1.176\times10^{-2}$ (-8.6%). Over $t\in[0,20]$ s, the mean absolute error (MAE) of ε is smaller for KM than GM (KM: 4.75×10^{-4} ; GM: 7.46×10^{-4}), with SM much larger (1.38×10^{-3}). In short, KM matches the DNS peak time/value and the time history slightly better than GM.

Next, we examine the energy spectrum. At t=10 s (Fig. 13; high-k inset in Fig. 14), both KM and GM reproduce the low-k range; differences appear only at high wave numbers. Using the mean log-spectral error over $k \in [10, 30]$, KM is lower than GM by $\sim 10\%$ at t=10 s (KM 0.192 vs GM 0.213) and by $\sim 8\%$ on average over $t \in [8, 10]$ s (KM 0.199 vs GM 0.216; Fig. 15). Thus, the *a posteriori* evidence indicates a small but consistent edge of KM over GM in the dissipative (high-k) range while maintaining comparable accuracy elsewhere.

Finally, we note the computational cost of the different SGS models on a 64³ grid. The required wall-clock times were approximately 1.77 h for KM, 1.45 h for GM, and 1.20 h for SM. Although KM is

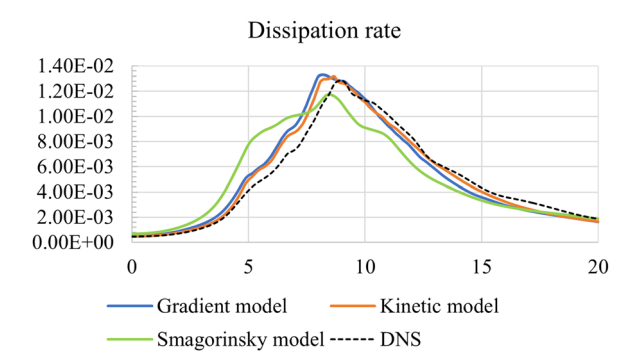


FIG. 12. Time evolution of the box-averaged dissipation rate $\varepsilon(t)$ in the Taylor–Green vortex at Re=1600. The horizontal axis denotes time t. The KM reproduces the DNS peak time and amplitude more accurately than the GM, while the Smagorinsky model underestimates dissipation.

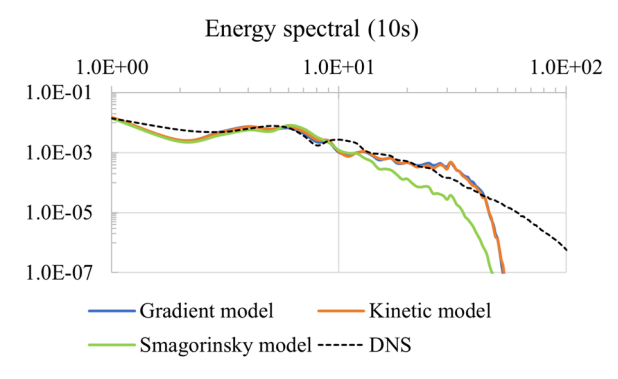


FIG. 13. Energy spectrum E(k) at t=10 s for the Taylor–Green vortex at Re=1600. The horizontal axis is the wavenumber k, and the vertical axis is the kinetic energy density. Both KM and GM reproduce the low-k range in agreement with DNS.

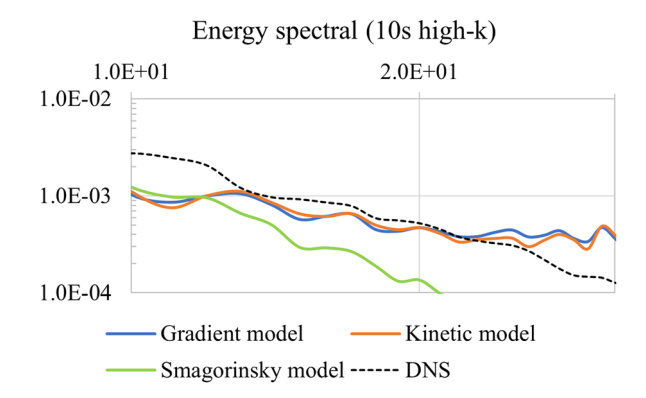


FIG. 14. Energy spectrum E(k) at t=10 s for the Taylor–Green vortex at Re=1600. The horizontal axis is the wavenumber k, and the vertical axis is the kinetic energy density. Differences appear at high k, where KM yields slightly better agreement with DNS than GM.

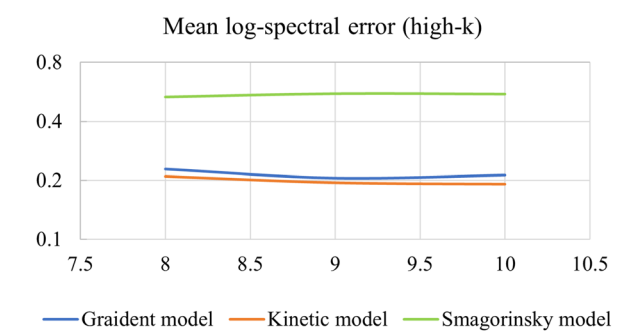


FIG. 15. Log-spectral error of the energy spectrum relative to DNS for $k \in [10, 32]$ during $t \in [8, 10]$ s. The horizontal axis denotes time t, and the vertical axis denotes the mean log-spectral error. KM shows consistently smaller errors than GM in the dissipative range, confirming the slight but systematic advantage of KM in a posteriori tests.

slightly more expensive than GM and SM, the additional cost is modest and may be justified by its improved stability and accuracy.

IV. CONCLUSION

In this study, we have deductively derived a parameter-free subgrid-scale (SGS) model from the error analysis of the lattice Boltzmann equation and validated its performance through both *a pri*ori and *a posteriori* tests. The main findings are summarized as follows.

First, in *a priori* tests using filtered DNS data, the evaluation based on the magnitude of the SGS volume force showed that the kinetic model reproduced the DNS reference more closely than the gradient model. From a local perspective, correlation coefficients and mean absolute errors (MAEs) indicated that GM slightly outperformed KM, whereas visual inspection of contour plots suggested that KM reproduced the global distribution more faithfully. When SGS dissipation was considered, GM again showed better local accuracy in terms of correlation and MAE, but KM exhibited superior global agreement with DNS when assessed through contour patterns and the autocorrelation function (ACF). ^{18,19}

Second, in the *a posteriori* validation using the Taylor–Green vortex at Re=1600, the KM consistently outperformed the GM in terms of dissipation rate and spectral analysis. Specifically, the KM reproduced the DNS peak dissipation at $t_p=8.673\,\mathrm{s}$ with $\varepsilon_p=1.316\times10^{-2}$, very close to the DNS value $\varepsilon_p^{\mathrm{DNS}}=1.286\times10^{-2}$ at $t_p^{\mathrm{DNS}}=8.97\,\mathrm{s}$. By contrast, the GM predicted an earlier peak at $t_p=8.152\,\mathrm{s}$ with $\varepsilon_p=1.331\times10^{-2}$, corresponding to a 3.5% overshoot. The time-averaged MAE of the dissipation rate was also smaller for KM (4.75×10^{-4}) than for GM (7.46×10^{-4}) . In the spectral domain, both models reproduced the low-k range accurately, but in the dissipative range $(k\in[10,30])$, KM yielded consistently lower log-spectral errors than GM $(0.192\,\mathrm{vs}\,0.213\,\mathrm{at}\,t=10\,\mathrm{s};\,0.199\,\mathrm{vs}\,0.216\,\mathrm{on}$ average over $t\in[8,10]\,\mathrm{s})$. These results demonstrate that KM has a systematic advantage over GM, even in the Taylor–Green vortex, a canonical test case where the GM is generally considered strong. 21,222

Third, the mathematical form of KM includes a hyperviscosity term, ²³ given by

$$F_{\alpha}^{\rm HV} = -\frac{\nu \Delta^2}{6} \sum_{\beta, \gamma} \frac{\partial^4 \overline{u}_{\alpha}}{\partial x^{\beta} \partial x^{\beta} \partial x^{\gamma} \partial x^{\gamma}}.$$
 (14)

The contribution of this term to the resolved kinetic energy budget is

$$\int_{\Omega} \overline{u}_{\alpha} F_{\alpha}^{\text{HV}} dV = -\frac{\nu \Delta^{2}}{6} \int_{\Omega} \overline{u}_{\alpha} \nabla^{4} \overline{u}_{\alpha} dV. \tag{15}$$

Applying integration by parts twice and assuming periodic boundaries (or vanishing fluxes), we obtain

$$\int_{\Omega} \overline{u}_{\alpha} F_{\alpha}^{\text{HV}} dV = -\frac{\nu \Delta^2}{6} \int_{\Omega} (\nabla^2 \overline{u}_{\alpha})^2 dV \le 0.$$
 (16)

Thus, the hyperviscosity term always provides a non-positive contribution to the resolved energy balance, i.e., it is strictly dissipative. Therefore, KM ensures numerical stability by preventing spurious energy backscatter, which explains its enhanced robustness compared with GM.

In addition, it should be noted that the remaining parts of the SGS volume force in Eq. (3), other than the hyperviscosity, can be written as gradients of scalar potentials. Such gradient terms may influence the local distribution of dissipation, but their volume integral reduces to a surface flux that vanishes under periodic or homogeneous boundary conditions. Consequently, they do not contribute to the net dissipation, and the strictly dissipative effect originates solely from the hyperviscosity term.

Finally, although the present analysis was restricted to isotropic turbulence and the Taylor–Green vortex, the lattice Boltzmann method is inherently based on a cubic lattice, which limits immediate application to wall-bounded flows. Nevertheless, recent developments^{24–27} of rectangular-grid and non-uniform lattice formulations suggest that extension of the present model to more general flow configurations is technically feasible. Our future work will, therefore, focus on incorporating such lattice refinements and assessing the applicability of the deductive SGS model to complex wall-bounded turbulence.

ACKNOWLEDGMENTS

We would like to thank Mr. Nozaki of IDAJ Co., Ltd. for practical advice regarding the configuration and execution of the Taylor–Green vortex simulations used for the *a posteriori* tests.

AUTHOR DECLARATIONS Conflict of Interest

The author has no conflicts to disclose.

Author Contributions

K. Yamamoto: Conceptualization (equal); Data curation (equal); Formal analysis (equal); Investigation (equal); Methodology (equal); Validation (equal); Visualization (equal); Writing – original draft (equal).

DATA AVAILABILITY

The data that support the findings of this study are available from the corresponding author upon reasonable request.

APPENDIX: DERIVATION OF THE KINETIC MODEL

Here, we derive the kinetic model from the LBE. As established in the literature, ¹² the distribution function is expressed as a power series of δ_t , and each undetermined coefficient is defined as follows:

$$f_i = f_i^{(0)} + \delta_t f_i^{(1)} + \delta_t^2 f_i^{(2)} + \delta_t^3 f_i^{(3)} + \cdots$$
 (A1)

The equation to be solved is the LBE shown as follows:

$$f_i(x + c_i\delta_t, t + \delta_t) - f_i(x, t) = -\frac{1}{\omega} \left(f_i - f_i^{eq} \right). \tag{A2}$$

By Taylor-expanding the left-hand side of Eq. (A2) and formally substituting Eq. (A2), we obtain the following evolution equation for the distribution function:

$$\hat{D}_{i}f_{i}^{(0)} + \delta_{t} \left(\frac{1}{2}\hat{D}_{i}^{2}f_{i}^{(0)} + \hat{D}_{i}f_{i}^{(1)}\right) + \delta_{t}^{2} \left(\frac{1}{6}\hat{D}_{i}^{3}f_{i}^{(0)} + \frac{1}{2}\hat{D}_{i}^{2}f_{i}^{(1)} + \hat{D}_{i}f_{i}^{(2)}\right) \\
+ \delta_{t}^{3} \left(\frac{1}{24}\hat{D}_{i}^{4}f_{i}^{(0)} + \frac{1}{6}\hat{D}_{i}^{3}f_{i}^{(1)} + \frac{1}{2}\hat{D}_{i}^{2}f_{i}^{(2)} + \hat{D}_{i}f_{i}^{(3)}\right) \\
= -\frac{1}{\omega} \left(f_{i}^{(1)} + \delta_{t}f_{i}^{(2)} + \delta_{t}^{2}f_{i}^{(3)} + \delta_{t}^{3}f_{i}^{(4)} + \cdots\right). \tag{A3}$$

By rearranging terms by the degree of δ_t , we obtain the following relationship that holds for each order:

$$\delta_t^0 : 0 = f_i^{(0)} - f_i^{eq}, \tag{A4}$$

$$\delta_t^1 : \hat{D}_i f_i^{(0)} = -\frac{1}{\alpha} f_i^{(1)},$$
 (A5)

$$\delta_t^2 : \frac{1}{2} \hat{D}_i^2 f_i^{(0)} + \hat{D}_i f_i^{(1)} = -\frac{1}{\omega} f_i^{(2)}, \tag{A6}$$

$$\delta_t^3 : \frac{1}{6} \hat{D}_i^3 f_i^{(0)} + \frac{1}{2} \hat{D}_i^2 f_i^{(1)} + \hat{D}_i f_i^{(2)} = -\frac{1}{\omega} f_i^{(3)}, \tag{A7}$$

$$\delta_t^4 : \frac{1}{24} \hat{D}_i^4 f_i^{(0)} + \frac{1}{6} \hat{D}_i^3 f_i^{(1)} + \frac{1}{2} \hat{D}_i^2 f_i^{(2)} + \hat{D}_i f_i^{(3)} = -\frac{1}{\omega} f_i^{(4)}. \tag{A8}$$

From the aforementioned equation, we express the undetermined coefficients of each degree of δ_t using only the zeroth-order distribution function, yielding the following:

$$f_i^{(1)} = -\varphi \hat{D}_i f_i^{(0)},\tag{A9}$$

$$f_i^{(2)} = \varphi\left(\varphi - \frac{1}{2}\right) = \frac{2\varphi^2 - \varphi}{2}\hat{D}_i^2 f_i^{(0)},$$
 (A10)

$$f_i^{(3)} = \frac{-6\varphi^3 + 6\varphi^2 - \varphi}{6} \hat{D}_i^3 f_i^{(0)}, \tag{A11}$$

$$f_i^{(4)} = \frac{24\varphi^4 - 36\varphi^3 + 14\varphi^2 - \varphi}{24} \hat{D}_i^4 f_i^{(0)}.$$
 (A12)

Substituting the above into Eq. (A3), we write the evolution equation using only the zeroth-order distribution function and obtain the following:

$$\sum_{i} \hat{D}_{i} f_{i}^{(0)} c_{i,\alpha} + \sum_{i} \delta_{t} \frac{-2\varphi + 1}{2} \hat{D}_{i}^{2} f_{i}^{(0)} c_{i,\alpha} + \sum_{i} \delta_{t}^{2} \frac{6\varphi^{2} - 6\varphi + 1}{6}$$

$$\times \hat{D}_{i}^{3} f_{i}^{(0)} c_{i,\alpha} + \sum_{i} \delta_{t}^{3} \frac{-24\varphi^{3} + 36\varphi^{2} - 14\varphi + 1}{24} \hat{D}_{i}^{4} f_{i}^{(0)} c_{i,\alpha} = 0.$$
(A13)

By explicitly expanding Eq. (A13), we obtain the following. Here, the third-order term of δ_t corresponds to the third order of Δ , but when the viscosity is large, only the last fourth-power term of c can be regarded as the square of Δ . Therefore, we do not ignore it here,

$$\sum_{i} \hat{D}_{i} f_{i}^{(0)} c_{i,\alpha} + \sum_{i} \delta_{t} \frac{-2\varphi + 1}{2} \hat{D}_{i}^{2} f_{i}^{(0)} c_{i,\alpha}$$

$$+ \sum_{i} \delta_{t}^{2} \frac{6\varphi^{2} - 6\varphi + 1}{6} \frac{\partial}{\partial x^{\beta}} \frac{\partial}{\partial x^{\gamma}} \frac{\partial}{\partial x^{\delta}} c_{i,\alpha} c_{i,\beta} c_{i,\gamma} c_{i,\delta} f_{i}^{(0)}$$

$$+ \sum_{i} \delta_{t}^{2} \frac{6\varphi^{2} - 6\varphi + 1}{6} 3 \frac{\partial}{\partial x^{\beta}} \frac{\partial}{\partial x^{\gamma}} \frac{\partial}{\partial t} c_{i,\alpha} c_{i,\beta} c_{i,\gamma} f_{i}^{(0)}$$

$$+ \sum_{i} \delta_{t}^{2} \frac{6\varphi^{2} - 6\varphi + 1}{6} 3 \frac{\partial}{\partial x^{\beta}} \frac{\partial}{\partial t} \frac{\partial}{\partial t} c_{i,\alpha} c_{i,\beta} f_{i}^{(0)}$$

$$+ \sum_{i} \delta_{t}^{2} \frac{6\varphi^{2} - 6\varphi + 1}{6} \frac{\partial}{\partial t} \frac{\partial}{\partial t} c_{i,\alpha} c_{i,\beta} f_{i}^{(0)}$$

$$+ \sum_{i} \delta_{t}^{3} \frac{-24\varphi^{3} + 36\varphi^{2} - 14\varphi + 1}{24}$$

$$\times \frac{\partial}{\partial x^{\beta}} \frac{\partial}{\partial x^{\gamma}} \frac{\partial}{\partial x^{\delta}} \frac{\partial}{\partial x^{\delta}} \frac{\partial}{\partial x^{\delta}} c_{i,\alpha} c_{i,\beta} c_{i,\gamma} c_{i,\delta} c_{i,\varepsilon} f_{i}^{(0)} = 0. \tag{A14}$$

The aforementioned equation can be transformed as follows for the quadratic term of Δ . The first equation uses Euler's equation, and the second accounts for the fact that the order is the square of $\left(\Delta/c\right)^2$,

$$\begin{split} &\sum_{i} \delta_{t}^{2} \frac{6\varphi^{2} - 6\varphi + 1}{6} \frac{\partial}{\partial x^{\beta}} \frac{\partial}{\partial x^{\gamma}} \frac{\partial}{\partial x^{\delta}} c_{i,\alpha} c_{i,\beta} c_{i,\gamma} c_{i,\delta} f_{i}^{(0)} \\ &+ \sum_{i} \delta_{t}^{2} \frac{6\varphi^{2} - 6\varphi + 1}{6} 3 \frac{\partial}{\partial x^{\beta}} \frac{\partial}{\partial x^{\gamma}} \frac{\partial}{\partial t} c_{i,\alpha} c_{i,\beta} c_{i,\gamma} f_{i}^{(0)} \\ &+ \sum_{i} \delta_{t}^{2} \frac{6\varphi^{2} - 6\varphi + 1}{6} 2 \frac{\partial}{\partial x^{\beta}} \frac{\partial}{\partial t} \frac{\partial}{\partial t} c_{i,\alpha} c_{i,\beta} f_{i}^{(0)} \\ &+ \frac{\partial}{\partial t} \frac{\partial}{\partial t} \sum_{i} \delta_{t}^{2} \frac{6\varphi^{2} - 6\varphi + 1}{6} \left(\frac{\partial}{\partial x^{\beta}} c_{i,\alpha} c_{i,\beta} + \frac{\partial}{\partial t} c_{i,\alpha} \right) f_{i}^{(0)} \\ &= \sum_{i} \delta_{t}^{2} \frac{6\varphi^{2} - 6\varphi + 1}{6} \frac{\partial}{\partial x^{\beta}} \frac{\partial}{\partial x^{\gamma}} \frac{\partial}{\partial x^{\delta}} c_{i,\alpha} c_{i,\beta} c_{i,\gamma} c_{i,\delta} f_{i}^{(0)} \\ &+ \sum_{i} \delta_{t}^{2} \frac{6\varphi^{2} - 6\varphi + 1}{6} 3 \frac{\partial}{\partial x^{\beta}} \frac{\partial}{\partial x^{\gamma}} \frac{\partial}{\partial t} c_{i,\alpha} c_{i,\beta} c_{i,\gamma} f_{i}^{(0)} \\ &+ \delta_{t}^{2} \frac{6\varphi^{2} - 6\varphi + 1}{6} 2 \frac{\partial}{\partial x^{\beta}} \frac{\partial}{\partial t} \frac{\partial}{\partial t} (\rho u_{\alpha} u_{\beta} + p \delta_{\alpha\beta}) \\ &= \sum_{i} \delta_{t}^{2} \frac{6\varphi^{2} - 6\varphi + 1}{6} \frac{\partial}{\partial x^{\beta}} \frac{\partial}{\partial x^{\gamma}} \frac{\partial}{\partial t} c_{i,\alpha} c_{i,\beta} c_{i,\gamma} c_{i,\delta} f_{i}^{(0)} \\ &+ \sum_{i} \delta_{t}^{2} \frac{6\varphi^{2} - 6\varphi + 1}{6} \frac{\partial}{\partial x^{\beta}} \frac{\partial}{\partial x^{\gamma}} \frac{\partial}{\partial t} c_{i,\alpha} c_{i,\beta} c_{i,\gamma} c_{i,\delta} f_{i}^{(0)}. \end{split}$$
(A15)

We use the following expression for the equilibrium distribution function for D3Q27:

$$f_i^{eq} = \omega_i \rho \left(\frac{1}{c_s^2} \frac{p}{\rho} + \frac{c_{i,\mu} c_{i,\nu} u_{\mu} u_{\nu}}{2c_s^4} - \frac{u_{\mu} u_{\mu}}{2c_s^2} \right) + \omega_i \rho \left(\frac{c_{i,\mu} u_{\mu}}{c_s^2} \right). \tag{A16}$$

The following relational expression is obtained from the LBM: 13

$$\nu = c_s^2 \delta_t \left(\varphi - \frac{1}{2} \right) \to c^4 \delta_t^3 = \frac{6\nu}{2\varphi - 1} \Delta^2. \tag{A17}$$

The following relational expressions, though self-evident, are shown as follows:

$$\Delta = c\delta_t. \tag{A18}$$

The DNS calculation conditions used in this paper are

$$\Delta = 2\pi/1024 = 0.00614,\tag{A19}$$

$$\delta_t = 0.0002, \tag{A20}$$

$$\nu = 0.000\,185,$$
 (A21)

$$c = \Delta/\delta_t = 30.7, \tag{A22}$$

$$c_s = 30.7/\sqrt{3} = 17.7.$$
 (A23)

Using these conditions, the coefficients of Eq. (A14) are calculated as follows:

$$\varphi - \frac{1}{2} = 0.002\,95,\tag{A24}$$

$$\frac{6\varphi^2 - 6\varphi + 1}{6} = -\frac{1}{12},\tag{A25}$$

$$\frac{-12\varphi^2 + 12\varphi - 1}{4} = \frac{1}{2}.$$
 (A26)

Substituting these into Eq. (A14) and rearranging, we obtain the following:

$$\begin{split} &\sum_{i} \hat{D}_{i} f_{i}^{(0)} c_{i,\alpha} + \sum_{i} \delta_{t} \frac{-2\varphi + 1}{2} \hat{D}_{i}^{2} f_{i}^{(0)} c_{i,\alpha} \\ &- \frac{1}{4} \Delta^{2} \sum_{i} \omega_{i} e_{i,\alpha} e_{i,\beta} e_{i,\gamma} e_{i,\delta} \frac{\partial}{\partial x^{\beta}} \frac{\partial}{\partial x^{\gamma}} \frac{\partial}{\partial x^{\delta}} p \\ &- \frac{3}{8} \rho \Delta^{2} \sum_{i} \omega_{i} e_{i,\alpha} e_{i,\beta} e_{i,\gamma} e_{i,\delta} e_{i,\mu} e_{i,\nu} \frac{\partial}{\partial x^{\beta}} \frac{\partial}{\partial x^{\gamma}} \frac{\partial}{\partial x^{\delta}} u_{\mu} u_{\nu} \\ &+ \frac{1}{8} \rho \Delta^{2} \sum_{i} \omega_{i} e_{i,\alpha} e_{i,\beta} e_{i,\gamma} e_{i,\delta} \frac{\partial}{\partial x^{\beta}} \frac{\partial}{\partial x^{\gamma}} \frac{\partial}{\partial x^{\delta}} u_{\mu} u_{\mu} \\ &- \frac{3}{4} \rho \Delta^{2} \sum_{i} \omega_{i} e_{i,\alpha} e_{i,\beta} e_{i,\gamma} e_{i,\mu} \frac{\partial}{\partial x^{\beta}} \frac{\partial}{\partial x^{\gamma}} \frac{\partial}{\partial t} u_{\mu} \\ &+ \frac{3}{2} \rho \nu \Delta^{2} \sum_{i} \omega_{i} e_{i,\alpha} e_{i,\beta} e_{i,\gamma} e_{i,\beta} e_{i,\mu} e_{i,\nu} \frac{\partial}{\partial x^{\beta}} \frac{\partial}{\partial x^{\gamma}} \frac{\partial}{\partial x^{\delta}} \frac{\partial}{\partial x^{\gamma}} \frac{\partial}{\partial x^{\delta}} \frac{\partial}{\partial x^{\mu}} u_{\nu} = 0. \end{split}$$

The fourth- and sixth-order tensors in D3Q27 are calculated as follows: 14

$$\sum_{i} \omega_{i} e_{i,\alpha} e_{i,\beta} e_{i,\gamma} e_{i,\delta} = \frac{1}{9} \Delta^{(4)}_{\alpha\beta\gamma\delta}, \tag{A28}$$

$$\sum_{\cdot} \omega_{i} e_{i,\alpha} e_{i,\beta} e_{i,\gamma} e_{i,\delta} e_{i,\mu} e_{i,\nu} = \frac{1}{27} \Delta^{(6)}_{\alpha\beta\gamma\delta\mu\nu} - \frac{2}{9} \delta_{\alpha\beta\gamma\delta\mu\nu}. \tag{A29}$$

Using this equation, the sixth-order tensor appearing in the fourth term on the left-hand side of Eq. (A27) is calculated as follows:

$$\begin{split} &\frac{\partial}{\partial x^{\beta}} \frac{\partial}{\partial x^{\gamma}} \frac{\partial}{\partial x^{\delta}} u_{\mu} u_{\nu} \sum_{i} \omega_{i} e_{i,\alpha} e_{i,\beta} e_{i,\gamma} e_{i,\delta} e_{i,\mu} e_{i,\nu} \\ &= \frac{1}{27} \frac{\partial}{\partial x^{\beta}} \frac{\partial}{\partial x^{\gamma}} \frac{\partial}{\partial x^{\delta}} u_{\mu} u_{\nu} \Delta_{\alpha\beta\gamma\delta\mu\nu}^{(6)} - \frac{2}{9} \frac{\partial}{\partial x^{\beta}} \frac{\partial}{\partial x^{\gamma}} \frac{\partial}{\partial x^{\delta}} u_{\mu} u_{\nu} \delta_{\alpha\beta\gamma\delta\mu\nu} \\ &= \frac{2}{9} \frac{\partial}{\partial x^{\beta}} \frac{\partial}{\partial x^{\gamma}} \frac{\partial}{\partial x^{\gamma}} (u_{\alpha} u_{\beta}) + \frac{1}{9} \frac{\partial}{\partial x^{\alpha}} \frac{\partial}{\partial x^{\beta}} \frac{\partial}{\partial x^{\beta}} (u_{\gamma} u_{\gamma}) \\ &+ \frac{2}{9} \frac{\partial}{\partial x^{\alpha}} \frac{\partial}{\partial x^{\beta}} \frac{\partial}{\partial x^{\gamma}} (u_{\beta} u_{\gamma}) - \frac{2}{9} \left(\frac{\partial}{\partial x^{\alpha}}\right)^{3} u_{\alpha}^{2}. \end{split} \tag{A30}$$

Similarly, the sixth-order tensor appearing in the seventh term on the left-hand side of Eq. (A27) is calculated as follows:

$$\begin{split} &\sum_{i} \omega_{i} e_{i,\alpha} e_{i,\beta} e_{i,\gamma} e_{i,\delta} e_{i,\mu} e_{i,\nu} \rho u_{\nu} \\ &= \frac{1}{27} \frac{\partial}{\partial x^{\beta}} \frac{\partial}{\partial x^{\gamma}} \frac{\partial}{\partial x^{\delta}} \frac{\partial}{\partial x^{\mu}} \rho u_{\nu} \Delta_{\alpha\beta\gamma\delta\mu\nu}^{(6)} - \frac{2}{9} \frac{\partial}{\partial x^{\beta}} \frac{\partial}{\partial x^{\gamma}} \frac{\partial}{\partial x^{\delta}} \frac{\partial}{\partial x^{\mu}} \rho u_{\nu} \delta_{\alpha\beta\gamma\delta\mu\nu} \\ &= \frac{1}{27} \left(12 \frac{\partial}{\partial x^{\alpha}} \frac{\partial}{\partial x^{\beta}} \frac{\partial}{\partial x^{\beta}} \frac{\partial}{\partial x^{\gamma}} \rho u_{\gamma} \right) + \frac{1}{27} \left(3 \frac{\partial}{\partial x^{\beta}} \frac{\partial}{\partial x^{\beta}} \frac{\partial}{\partial x^{\gamma}} \frac{\partial}{\partial x^{\gamma}} \rho u_{\alpha} \right) \\ &- \frac{2}{9} \left(\frac{\partial}{\partial x^{\alpha}} \right)^{4} (\rho u_{\alpha}) \\ &= \frac{1}{9} \frac{\partial}{\partial x^{\beta}} \frac{\partial}{\partial x^{\beta}} \frac{\partial}{\partial x^{\gamma}} \frac{\partial}{\partial x^{\gamma}} \rho u_{\alpha} - \frac{2}{9} \left(\frac{\partial}{\partial x^{\alpha}} \right)^{4} (\rho u_{\alpha}). \end{split} \tag{A31}$$

Substituting Eqs. (A28), (A30), and (A31) into Eq. (A27) and rearranging, we obtain the following:

$$\begin{split} &\sum_{i} \hat{D}_{i} f_{i}^{(0)} c_{i,\alpha} + \sum_{i} \delta_{t} \frac{-2\varphi + 1}{2} \hat{D}_{i}^{2} f_{i}^{(0)} c_{i,\alpha} + \frac{\rho \Delta^{2}}{12} \\ &\times \left\{ \frac{\partial}{\partial x^{\alpha}} \frac{\partial}{\partial x^{\gamma}} \frac{\partial}{\partial x^{\mu}} (u_{\mu} u_{\gamma}) + 2 \frac{\partial}{\partial x^{\alpha}} \frac{\partial}{\partial x^{\gamma}} \frac{\partial}{\partial x^{\gamma}} \frac{\rho}{\rho} \right\} + \frac{\rho \Delta^{2}}{12} \left(\frac{\partial}{\partial x^{\alpha}} \right)^{3} u_{\alpha}^{2} \\ &+ \frac{\rho \nu \Delta^{2}}{6} \left\{ \frac{\partial}{\partial x^{\beta}} \frac{\partial}{\partial x^{\beta}} \frac{\partial}{\partial x^{\beta}} \frac{\partial}{\partial x^{\gamma}} \frac{\partial}{\partial x^{\gamma}} u_{\alpha} - 2 \left(\frac{\partial}{\partial x^{\alpha}} \right)^{4} u_{\alpha} \right\} = 0. \end{split} \tag{A32}$$

The usual Navier–Stokes equation can be obtained from the first and second terms of Eq. (A32), but here, we confirm this and ensure that no extra terms corresponding to the turbulence model are generated. By writing out the first and second terms of Eq. (A32) and expanding them, we obtain the following equation:

$$\sum_{i} \hat{D}_{i} f_{i}^{(0)} c_{i,\alpha} + \sum_{i} \delta_{t} \frac{-2\varphi + 1}{2} \hat{D}_{i}^{2} f_{i}^{(0)} c_{i,\alpha}$$

$$= \frac{\partial \rho u_{\alpha}}{\partial t} + \frac{\partial}{\partial x^{\beta}} (\rho u_{\alpha} u_{\beta} + p \delta_{\alpha\beta})$$

$$+ \sum_{i} \delta_{t} \frac{-2\varphi + 1}{2} \frac{\partial}{\partial x^{\beta}} \frac{\partial}{\partial x^{\gamma}} c_{i,\alpha} c_{i,\beta} c_{i,\gamma} f_{i}^{(0)}$$

$$+ \delta_{t} \frac{-2\varphi + 1}{2} \frac{\partial}{\partial t} \sum_{i} \left(\frac{\partial}{\partial x^{\beta}} c_{i,\beta} + \frac{\partial}{\partial t} \right) c_{i,\alpha} f_{i}^{(0)}$$

$$+ \sum_{i} \delta_{t} \frac{-2\varphi + 1}{2} \frac{\partial}{\partial x^{\beta}} \frac{\partial}{\partial t} c_{i,\alpha} c_{i,\beta} f_{i}^{(0)}.$$
(A33)

As the second term on the right-hand side of Eq. (A33) does not include a time derivative and cannot yield a turbulence model, the results are shown as follows with reference to Ref. 13:

$$\begin{split} \sum_{i} \delta_{t} \frac{-2\varphi + 1}{2} \frac{\partial}{\partial x^{\beta}} \frac{\partial}{\partial x^{\gamma}} c_{i,\alpha} c_{i,\beta} c_{i,\gamma} f_{i}^{(0)} \\ &= \delta_{t} \frac{-2\varphi + 1}{2} \left\{ \frac{\partial c_{s}^{2} \rho u_{\gamma}}{\partial x^{\gamma}} \delta_{\alpha\beta} + c_{s}^{2} \rho \left(\frac{\partial u_{\beta}}{\partial x_{\alpha}} + \frac{\partial u_{\alpha}}{\partial x_{\beta}} \right) \right. \\ &+ \frac{\partial c_{s}^{2} \rho}{\partial x^{\alpha}} u_{\beta} + \frac{\partial c_{s}^{2} \rho}{\partial x^{\beta}} u_{\alpha} \right\}. \end{split} \tag{A34}$$

As the third term on the right-hand side of Eq. (A33) contains a time derivative, we approximate it using the Navier–Stokes equation to obtain the following result:

$$\begin{split} &\delta_{t} \frac{-2\varphi + 1}{2} \frac{\partial}{\partial t} \sum_{i} \left(\frac{\partial}{\partial x^{\beta}} c_{i,\beta} + \frac{\partial}{\partial t} \right) c_{i,\alpha} f_{i}^{(0)} \\ &= \delta_{t} \frac{-2\varphi + 1}{2} \frac{\partial}{\partial t} \left\{ \frac{\partial \rho u_{\alpha}}{\partial t} + \frac{\partial}{\partial x^{\beta}} (\rho u_{\alpha} u_{\beta} + p \delta_{\alpha\beta}) \right\} \\ &= \delta_{t} \frac{-2\varphi + 1}{2} \frac{\partial}{\partial t} \eta \left(\frac{\partial u_{\beta}}{\partial x_{\alpha}} + \frac{\partial u_{\alpha}}{\partial x_{\beta}} \right). \end{split} \tag{A35}$$

The aforementioned term is the viscous term multiplied by the viscosity and the value of Eq. (A24), which is very small relative to the viscous term and, therefore, can be neglected. This also shows that if the time derivative is approximated using the NS equation instead of the Euler equation, the viscosity term is multiplied by a very small value, making it acceptable to use the Euler equation in practice.

From this consideration, it follows that the time derivative of the fourth term on the right-hand side of Eq. (A33) can also be approximated by the Euler equation, and the following result is obtained from Ref. 13:

$$\begin{split} &\sum_{i} \delta_{t} \frac{-2\varphi + 1}{2} \frac{\partial}{\partial x^{\beta}} \frac{\partial}{\partial t} c_{i,\alpha} c_{i,\beta} f_{i}^{(0)} \\ &= \delta_{t} \frac{-2\varphi + 1}{2} \frac{\partial}{\partial x^{\beta}} \frac{\partial}{\partial t} \left(\rho u_{\alpha} u_{\beta} + p \delta_{\alpha\beta} \right) \\ &= \delta_{t} \frac{-2\varphi + 1}{2} \frac{\partial}{\partial x^{\beta}} \left(-\frac{\partial p}{\partial x^{\alpha}} u_{\beta} - \frac{\partial p}{\partial x^{\beta}} u_{\alpha} - \frac{\partial \rho u_{\alpha} u_{\beta} u_{\gamma}}{\partial x^{\gamma}} + \frac{\partial p}{\partial t} \delta_{\alpha\beta} \right) \\ &+ \delta_{t} \frac{-2\varphi + 1}{2} \frac{\partial}{\partial x^{\beta}} \left(-\frac{\partial p}{\partial x^{\alpha}} u_{\beta} - \frac{\partial p}{\partial x^{\beta}} u_{\alpha} - \frac{\partial c_{s}^{2} \rho u_{\gamma}}{\partial x^{\gamma}} \right) \\ &+ \delta_{t} \frac{-2\varphi + 1}{2} \frac{\partial}{\partial x^{\beta}} \left(-\frac{2}{3} c_{s}^{2} \rho \frac{\partial u_{\gamma}}{\partial x^{\gamma}} \delta_{\alpha\beta} \right) \\ &+ \delta_{t} \frac{-2\varphi + 1}{2} \frac{\partial}{\partial x^{\beta}} \left(-\frac{\partial \rho u_{\alpha} u_{\beta} u_{\gamma}}{\partial x^{\gamma}} \right). \end{split} \tag{A36}$$

By substituting Eqs. (A35), (A36), and (A37) into Eq. (A32), the following equation is obtained, confirming the derivation of the kinetic model:

$$\begin{split} \frac{\partial u_{\alpha}}{\partial t} + u_{\beta} \frac{\partial u_{\alpha}}{\partial x^{\beta}} &= -\frac{\partial}{\partial x^{\alpha}} \left(\frac{p}{\rho} \right) + \nu \frac{\partial}{\partial x^{\beta}} \left(\frac{\partial u_{\beta}}{\partial x^{\alpha}} + \frac{\partial u_{\alpha}}{\partial x^{\beta}} \right) - \frac{\Delta^{2}}{12} \\ &\times \left\{ \frac{\partial}{\partial x^{\alpha}} \frac{\partial}{\partial x^{\gamma}} \frac{\partial}{\partial x^{\mu}} (u_{\mu} u_{\gamma}) + 2 \frac{\partial}{\partial x^{\alpha}} \frac{\partial}{\partial x^{\gamma}} \frac{p}{\partial x^{\gamma}} \frac{p}{\rho} \right\} \\ &- \frac{\Delta^{2}}{12} \left(\frac{\partial}{\partial x^{\alpha}} \right)^{3} u_{\alpha}^{2} - \frac{\nu \Delta^{2}}{6} \left(\frac{\partial}{\partial x^{\beta}} \frac{\partial}{\partial x^{\beta}} \frac{\partial}{\partial x^{\gamma}} \right. \\ &\times \frac{\partial}{\partial x^{\gamma}} u_{\alpha} - 2 \left(\frac{\partial}{\partial x^{\alpha}} \right)^{4} u_{\alpha} \right). \end{split} \tag{A37}$$

REFERENCES

- ¹S. Chen and G. D. Doolen, "Lattice Boltzmann method for fluid flows," Annu. Rev. Fluid Mech. **30**, 329–364 (1998).
- ²M. Han, R. Ooka, and H. Kikumoto, "Lattice Boltzmann method-based large-eddy simulation of indoor isothermal airflow," Int. J. Heat Mass Transfer 130, 700–709 (2019).
- ³K. Yamamoto and T. Seta, "Derivation of multicomponent lattice Boltzmann equations by introducing a nonequilibrium distribution function into the Maxwell iteration based on the convective scaling," J. Stat. Phys. 182, 4 (2021).
- ⁴M. Geier, M. Schönherr, A. Pasquali, and M. Krafczyk, "The cumulant lattice Boltzmann equation in three dimensions: Theory and validation," Comput. Math. Appl. **70**, 507–547 (2015).
- ⁵G. G. Spinelli, T. Horstmann, K. Masilamani, M. M. Soni, H. Klimach, A. Stück, and S. Roller, "HPC performance study of different collision models using the Lattice Boltzmann solver Musubi," Comput. Fluids 255, 105833 (2023).
- ⁶R. D. van Valderen, B. E. Juarez-Garza, M. E. Klijn, M. Ottens, and C. Haringa, "Implicit large eddy simulations for hydrodynamic stress characterization in 125 mL shake flasks for stem cell cultures," <u>Biochem. Eng. J.</u> 219, 109734 (2025).
- ⁷H. Chen, S. Kandasamy, S. A. Orszag, R. Shock, S. Succi, and V. Yakhot, "Extended Boltzmann kinetic equation for turbulent flows," Science 301, 633–636 (2003).
- ⁸H. Chen, S. A. Orszag, I. Staroselsky, and S. Succi, "Analysis of subgrid scale turbulence using the Boltzmann Bhatnagar-Gross-Krook kinetic equation," Phys. Rev. E **59**, R2527–R2530 (1999).
- ⁹H. Chen, S. A. Orszag, I. Staroselsky, and S. Succi, "Expanded analogy between Boltzmann kinetic theory of fluids and turbulence," J. Fluid Mech. **519**, 301–314 (2004).
- ¹⁰M. E. Brachet, "Small-scale structure of the Taylor-Green vortex," J. Fluid Mech. 130, 411–452 (1983).
- ¹¹K. Suga, Y. Kuwata, K. Takashima, and R. Chikasue, "A D3Q27 multiple-relaxation-time lattice Boltzmann method for turbulent flows," Comput. Math. Appl. 69, 518–529 (2015).
- ¹²D. J. Holdych, D. R. Noble, J. G. Georgiadis, and R. O. Buckius, "Truncation error analysis of lattice Boltzmann methods," J. Comput. Phys. 193, 595–619 (2004).
- ¹³K. Yamamoto, "Novel expansion method for deriving the Navier-Stokes equation from the lattice Boltzmann equation," Multiphase Sci. Technol. 34, 35–45 (2022).
- ¹⁴M. Watari and M. Tsuahara, "Possibility of constructing a multispeed Bhatnagar-Gross-Krook thermal model of the lattice Boltzmann method," Phys. Rev. E 70, 016703 (2004).
- ¹⁵F. Hamba, "Scale-space energy density for inhomogeneous turbulence based on filtered velocities," J. Fluid Mech. 931, A34 (2022).
- 16Y. Li, E. Perlman, M. Wan, Y. Yang, C. Meneveau, R. Burns, S. Chen, A. Szalay, and G. Eyink, "A public turbulence database cluster and applications to study Lagrangian evolution of velocity increments in turbulence," J. Turbul. 9, N31 (2008).
- 17 A. Giauque, C. Giguet, A. Vadrot, and C. Corre, "A priori test of Large-Eddy Simulation models for the Sub-Grid Scale turbulent stress tensor in perfect and transcritical compressible real gas Homogeneous Isotropic Turbulence," Comput. Fluids 268, 106091 (2024).
- ¹⁸D. Xavier, S. Rezaeiravesh, and P. Schlatter, "Autoregressive models for quantification of time-averaging uncertainties in turbulent flows," Phys. Fluids 36, 105122 (2024).
- ¹⁹S. K. Jena and R. Manceau, "Dynamics of turbulent natural convection in a cubic cavity with centrally placed partially heated inner obstacle," Phys. Fluids 36, 085123 (2024).
- ²⁰S. D. Tullio, M. Napolitano, F. Ubertini, and F. Picano, "An OpenFOAM solver for multiphase and turbulent flow with immersed boundary method," Phys. Fluids 32, 043303 (2020).
- ²¹A. Prakash, K. Bhattacharya, and M. Ihme, "Optimal clipping of structural subgrid stress for large-eddy simulations," arXiv:2201.09122 (2022).
- grid stress for large-eddy simulations," arXiv:2201.09122 (2022).

 22 M. Klein, "Regularized, parameter-free scale similarity type models for large-eddy simulation," Int. J. Heat Fluid Flow 81, 108496 (2020).
- ²³J.-L. Guermond and S. Prudhomme, "Mathematical analysis of a spectral hyperviscosity LES model for the simulation of turbulent flows," ESAIM 37, 893–908 (2003).

²⁴E. Yahia and K. N. Premnath, "Central moment lattice Boltzmann method on a rectangular lattice," Phys. Fluids 33, 057110 (2021).
²⁵C. Lyu, P. Liu, T. Hu, X. Geng, Q. Qu, T. Sun, and R. A. D. Akkermans, "Hybrid method for wall local refinement in lattice Boltzmann method simulation," Phys. Fluids 35, 017103 (2023).

²⁶Z.-W. He, C. Shu, and Z. Chen, "Simplified lattice Boltzmann method on multi-resolution mesh," Phys. Fluids 36, 087171 (2024).
²⁷Z. Guo, S. Zhang, Y. Zhu, and D. Li, "Phase-field lattice Boltzmann model with

adaptive mesh refinement for ferrofluid interfacial dynamics," Phys. Fluids 37, 022148 (2025).